Electronic Supplementary Information

A and B site co-doping of CaMnO₃: A Route to Enhance the Heat Storage Properties

Emanuela Mastronardo[1,2, a)], Xin Qian[3], Juan M. Coronado[2] and Sossina M. Haile[3, b)]

[1] *Engineering Department, University of Messina. C.da di Dio, 98126. Messina, Italy.*
[2] *Instituto de Catálisis y Petroleoquímica. CSIC. C/ Marie Curie, 2. E-28049. Madrid, Spain.*
[3] *Materials Science and Engineering, Northwestern University, 2220 Campus Drive Cook Hall, 60208 Evanston, IL, United States.*

Corresponding authors: [a)] emastronardo@unime.it

[b)] sossina.haile@northwestern.edu

1. Energy Dispersive X-Ray (EDX) Spectroscopy

EDX mapping was performed using an Oxford X-max 80 SDD in conjunction with scanning electron microscopy imaging (Hitachi SU8030) The images, **Figure S 1**, reveal the dopants Fe and La are homogeneously dispersed in both LCFM5 and LCFM10.
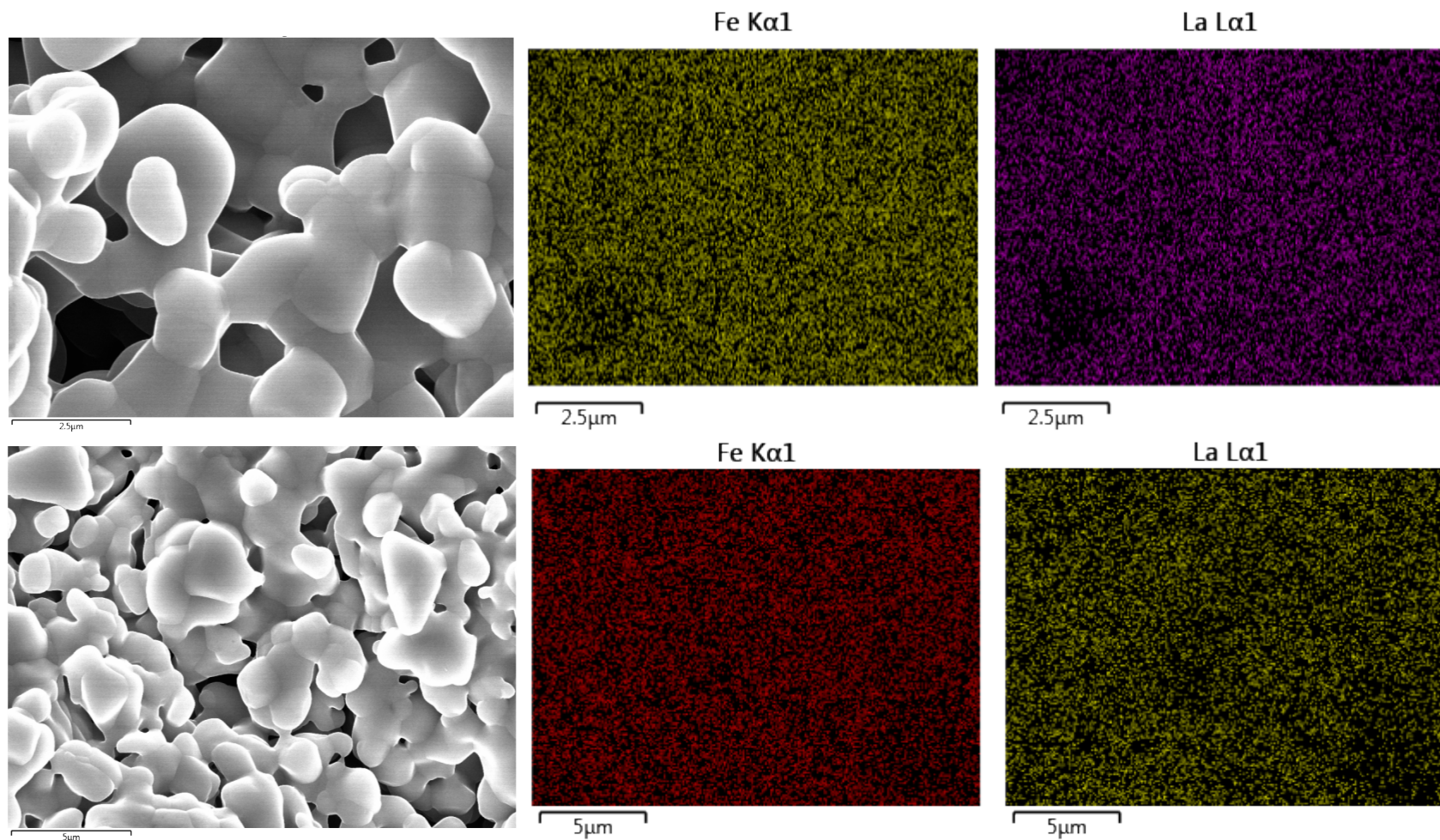

Figure S 1. EDX mapping of Fe and La in LCFM5 (upper row) and LCFM10 (lower row). Note the difference in scales.

1. X-Ray Diffraction

X-ray diffraction patterns were collected using a Rigaku Ultima IV diffractometer (Cu Ka, 40 v, 44 mA) over the 2Θ range 20° to 80° at a scan rate of 0.05°/s. The patterns of $CaMnO_3$, LCFM5 and LCFM10 are compared in Figure S 1a, with indexing according to an orthorhombic cell (space group Pnma, $GdFeO_3$-type structure); the results of Rietveld refinement are shown in **Figure S 2**b and **Figure S 2**c, respectively, for LCFM5 and LCFM10. Refinement was performed using the GSAS software package and the structure of $CaMnO_3$ as the initial model. Refinement parameters were limited to lattice parameters and sample displacement. Peak profile parameters were taken from an independent measurement using a LaB_6 reference. Chemical identities of the A and M site atoms were fixed at the target chemistries, as justified by the ICP chemical analysis. The data residual (Rwp), the R_{bragg}, and Goodness of Fit (GOF) are also reported in the graphs. Note the absence of the K_β peak from the patterns shown in **Figure 5** (main text), in which data were collected using a configuration that provided greater filtering of the Kβ radiation.
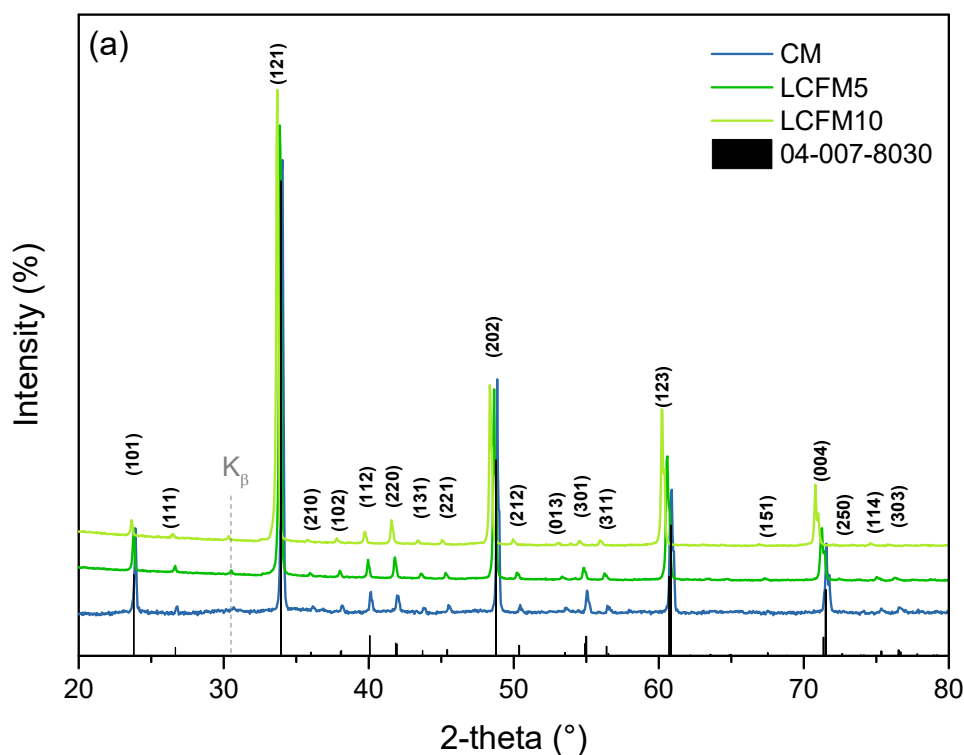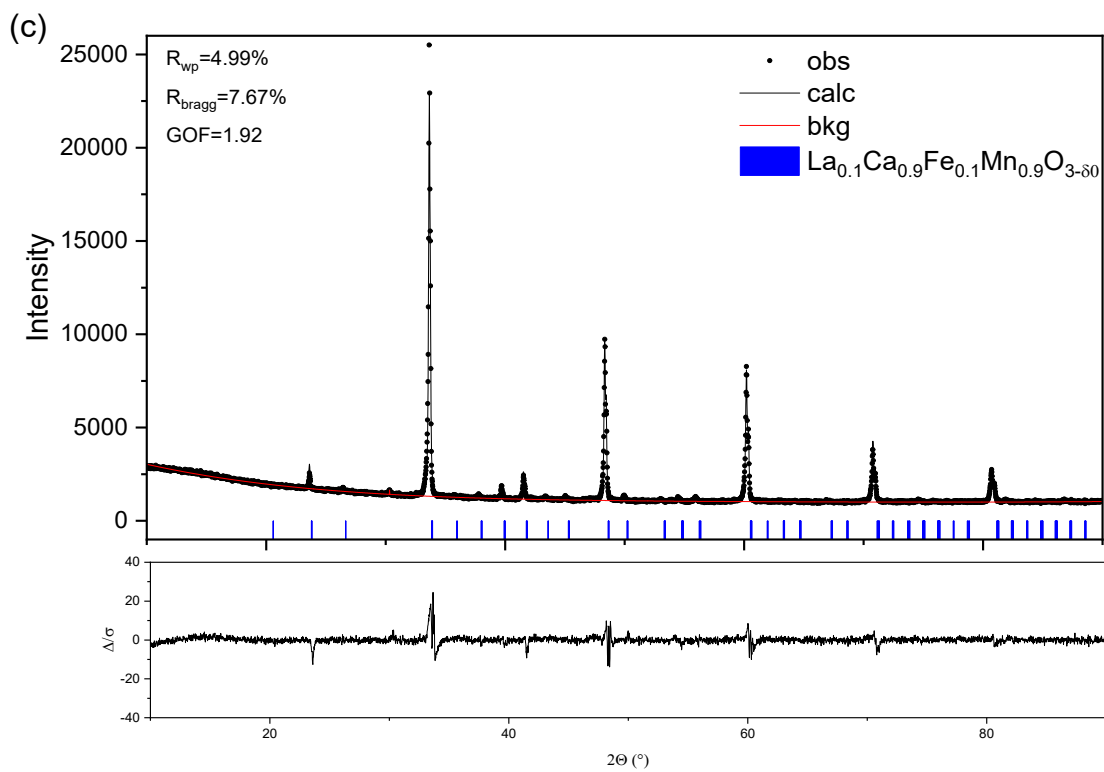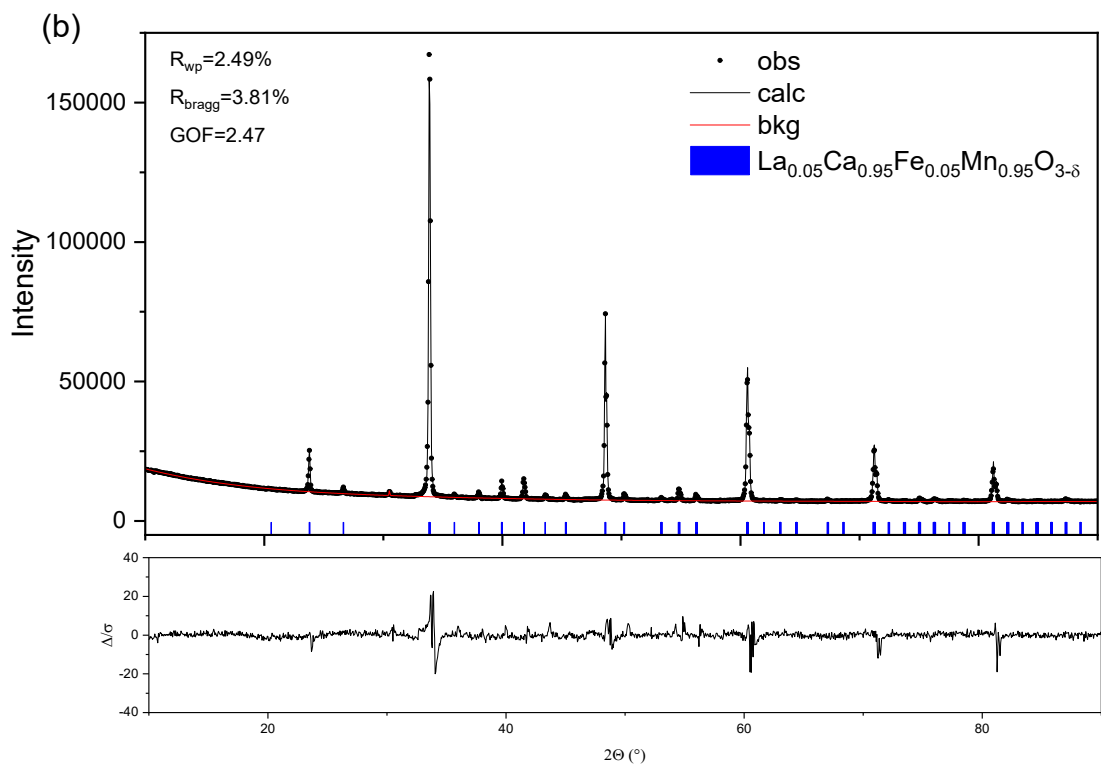
Figure S 2. (a) Comparison of XRD patterns of $CaMnO_3$, LCFM5, and LCFM10, as indicated; and comparison of measured and calculated patterns of (b) LCFM5 and (c) LCFM10 obtained from Rietveld refinement.

In the following tables are reported the atomic coordinates for LCFM5 and LCFM10 obtained by the refinement fixing Uiso, fraction, and atomic coordinates for both A-site cations and B-site cations:

Table S 1. Atomic coordinates for LCFM5.

Atom	site	x	y	z	Uiso	fraction
La3+	4c	0.49773	0.25	-0.0266	0.01	0.05
Ca2+	4c	0.49773	0.25	-0.0266	0.01	0.95
Fe3+	4b	0	0	0.5	0.01	0.05
Mn4+	4b	0	0	0.5	0.01	0.95
O2-	4c	0.51595	0.25	0.57385	0.01	1
O2-	8d	0.21388	0.02871	0.284	0.01	1

Table S 2. Atomic coordinates for LCFM10.

Atom	site	x	y	z	Uiso	fraction
La3+	4c	0.49717	0.25	-0.02173	0.01	0.1
Ca2+	4c	0.49717	0.25	-0.02173	0.01	0.9
Fe3+	4b	0	0	0.5	0.01	0.1
Mn3+	4b	0	0	0.5	0.01	0.9
O2-	4c	0.5154	0.25	0.55978	0.01	1
O2-	8d	0.214	0.0335	0.28171	0.01	1

2. XANES measurements

X-ray adsorption data were collected about the K-edges of Mn and Fe and about the L-III edge of La as a means of determining the oxidation states of these elements in the doped $CaMnO_3$ materials. The adsorption spectra were measured under ambient conditions (room temperature and synthetic air) in transmission mode from powder samples using the facilities at beamline 5BM-D of the Advanced Photon Source (APS) at Argonne National Laboratory. Shown in **Figure S 3** are the La spectra of the perovskites of this work in comparison to the La L-III edge of La_2O_3, taken from the database of the International X-ray Absorption Society [http://ixs.iit.edu/database/]. The edge energies of the three materials are identical, indicating that La is in the 3+ oxidation state in the perovskites.
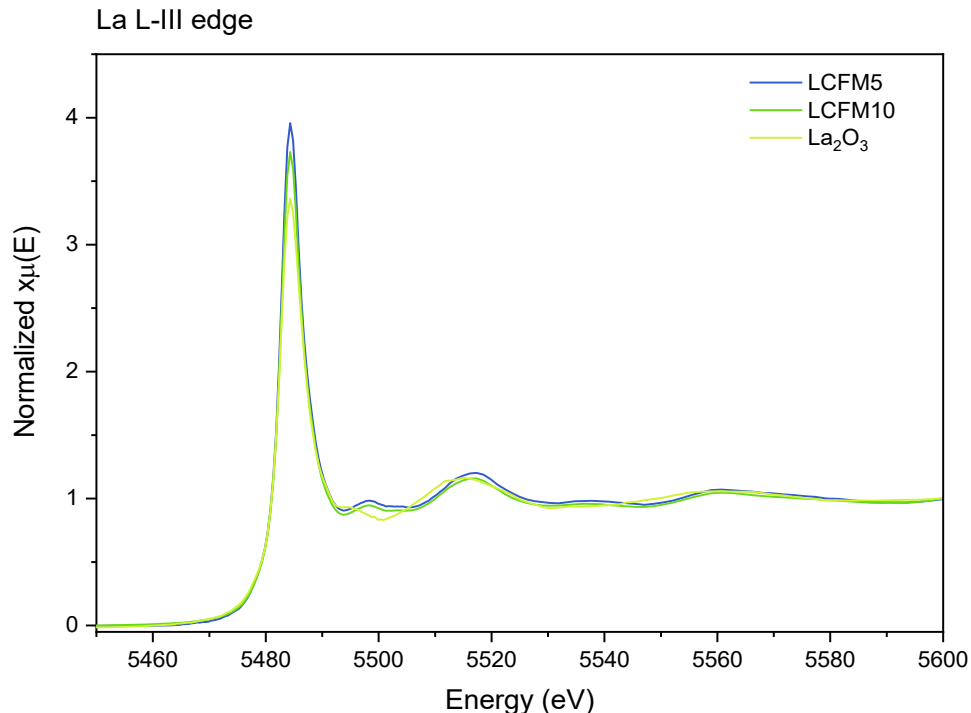

Figure S 3. La XANES spectra of LCFM5 and LCFM10. La_2O_3 as reference material is also included.

Linear calibration curves for converting the measured absorption edge energies for the K-edges of Mn and Fe in the doped $CaMnO_3$ materials were established from the XANES spectra of elemental Fe and of oxides of Mn and Fe available in the database of the International X-ray Absorption Society [http://ixs.iit.edu/database/]. The respective calibration lines are shown in Figure S 4, along with the edge positions measured for LCMF perovskites. Though the edge

positions of the perovskites are distinct, at both the Mn and especially the Fe edges (see **Table S 1** below), they are not distinguishable on the scale of the figures. The Mn edge positions in the perovskites are found to lie within 0.11 eV of that of MnO, indicating Mn is in the 4+ oxidation state. The Fe edge positions in the LCMF materials, including undoped LaFeO$_3$, are slightly above that of the Fe$_2$O$_3$, by 0.5 to 0.6 eV. As Fe^{4+} is an exceeding rare species, we conclude that Fe is fully in the 3+ oxidation state in LCMF, and the very small offset suggesting an oxidization state of 3.1+ is within experimental error.
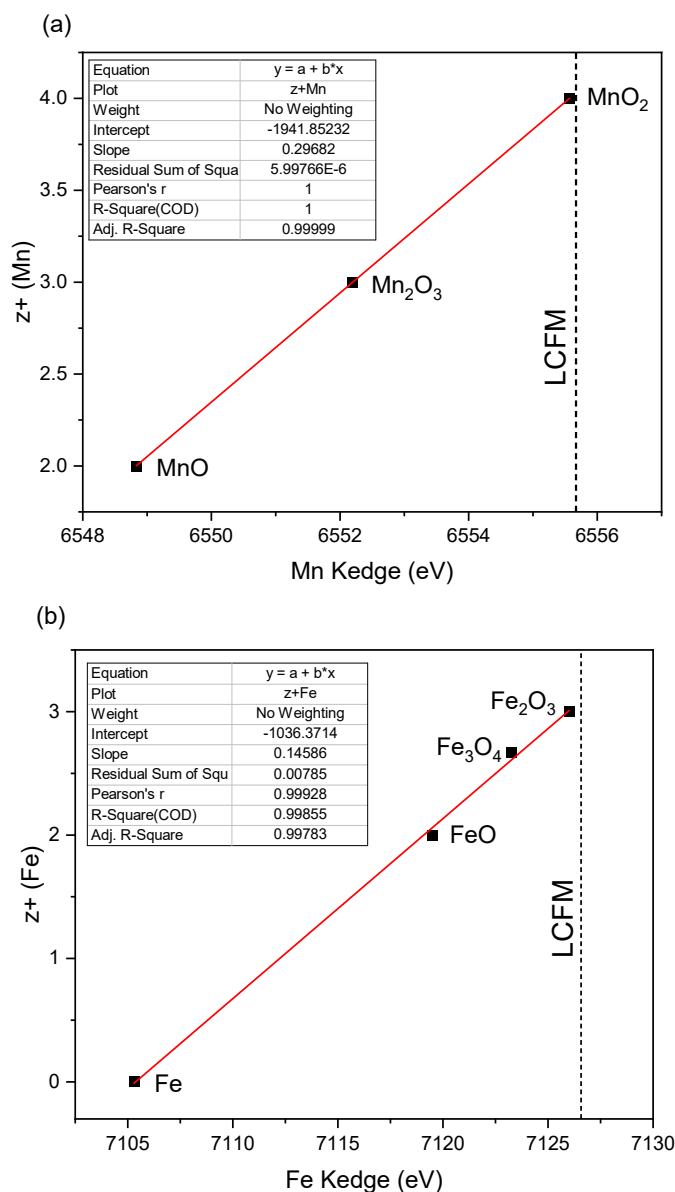

Figure S 4. Linear calibration curves for the determination of (a) Mn and (b) Fe oxidation states.

3. TGA measurement for thermodynamic data extraction

Thermogravimetric data were collected under controlled gas atmospheres using a simultaneous thermal analyzer (STA449 F5 Jupiter Netzsch) coupled with an inline pO_2 sensor (MicroPoas, Setnag) for measuring the oxygen partial pressure of the exhaust gas. The total flow rate was fixed at 250 mL/min. The sensor was placed downstream of the TGA in a sealed quartz tube, in turn, placed in a furnace held at a temperature of 700 °C. To prevent possible reaction between the material and the alumina sample holder of the STA at high temperatures, the latter was covered by Pt foil prior to placement of the sample. In **Figure S 5** is shown the temperature profile used for a typical experiment. Each experiment was again initiated with a 1 h hold under $pO_2 = 0.18$ atm to remove possible surface adsorbed species. Data were recorded at seven different pO_2 values: 0.18, 0.09, 0.07, 0.04, 0.02, 0.008, 0.004 atm.
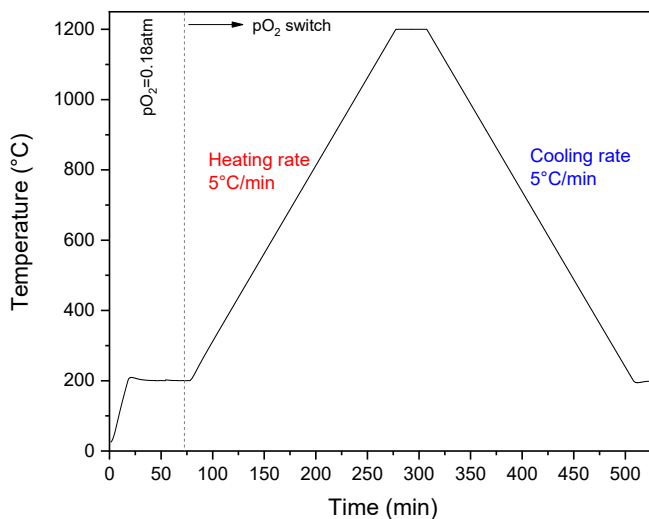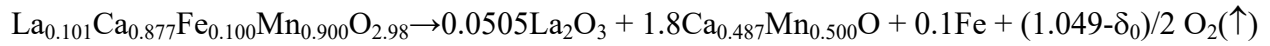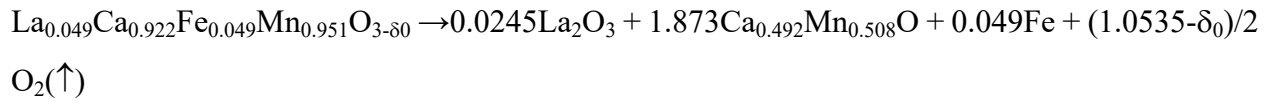

Figure S 5. Temperature profile of a typical TGA experiment.

4. TGA measurement of absolute oxygen non-stoichiometry

The oxygen non-stoichiometry in the as-prepared material (δ_0) was evaluated through complete reduction of the material at 1000 °C under 3%H_2/Ar flow with TGA measurement (**Figure S 6**a) and the residual composition has been analyzed by XRD (**Figure S 6**b). No mass loss occurred though the initial hold at 200 °C under $pO_2 = 0.21$ atm) (synthetic air), and based on comparison of the mass loss curves at two different oxygen partial pressures presented in Figure 7 and Figure 8, the masses at 200 °C and $pO_2 = 0.21$ atm and those at 200 °C and $pO_2 = 0.18$ atm (the reference state used in the TGA measurements) are safely approximately as equal. Thus, the d0 measured by the complete reduction experiment reflects the non-stoichiometry in the TGA reference state. After complete reduction the detected products are $Ca_{0.5}Mn_{0.5}O$, La_2O_3 and metallic Fe in different ratios. Accounting for the ICP measured cation ratios, the decomposition of LCFM5, for example, is taken to occur according to the following reaction:

$La_{0.049}Ca_{0.922}Fe_{0.049}Mn_{0.951}O_{3-\delta 0} \rightarrow 0.0245La_2O_3 + 1.873Ca_{0.492}Mn_{0.508}O + 0.049Fe + (1.0535-\delta_0)/2$ $O_2(\uparrow)$

$La_{0.101}Ca_{0.877}Fe_{0.100}Mn_{0.900}O_{2.98} \rightarrow 0.0505La_2O_3 + 1.8Ca_{0.487}Mn_{0.500}O + 0.1Fe + (1.049-\delta_0)/2\ O_2(\uparrow)$

There is slight uncertainty in the analysis because of the unknown final state of the Mn, which can be dissolved as Mn^{2+} in the rock salt oxide, $(Ca,Mn)O$, as written, or as Mn^0 in the Fe metal. At the reduction temperature of 1000 °C, the solubility limit of Mn in Fe is ~ 65 mol %[1], whereas MnO is completely miscible in CaO at this temperature[2], justifying the presumption of Mn incorporation solely in the oxide phase. Furthermore, the lattice parameters of the rocksalt products, 4.6310(2) and 4.6263(9) Å, respectively, from LCFM5 and LCFM10, are within error of the value of 4.6286 expected from linear interpolation between the respective lattice parameters of the CaO and MnO endmembers, 4.8112 [3] and 4.466(1) Å [3]. The full reduction of Fe to the metallic state while Mn remains an oxide suggests participation of Fe in the reduction of the perovskite phase. From the mass loss percentages of 11.2% and 11.0%, respectively, for LCFM5 and LCFM10, the respective δ_0 values are estimated to be 0.03 and 0.01, in agreement with the implied stoichiometry from ICP-MS analysis. Being within experimental error of 0, δ_0 is taken to be exactly 0 in the thermodynamic analysis of both materials.
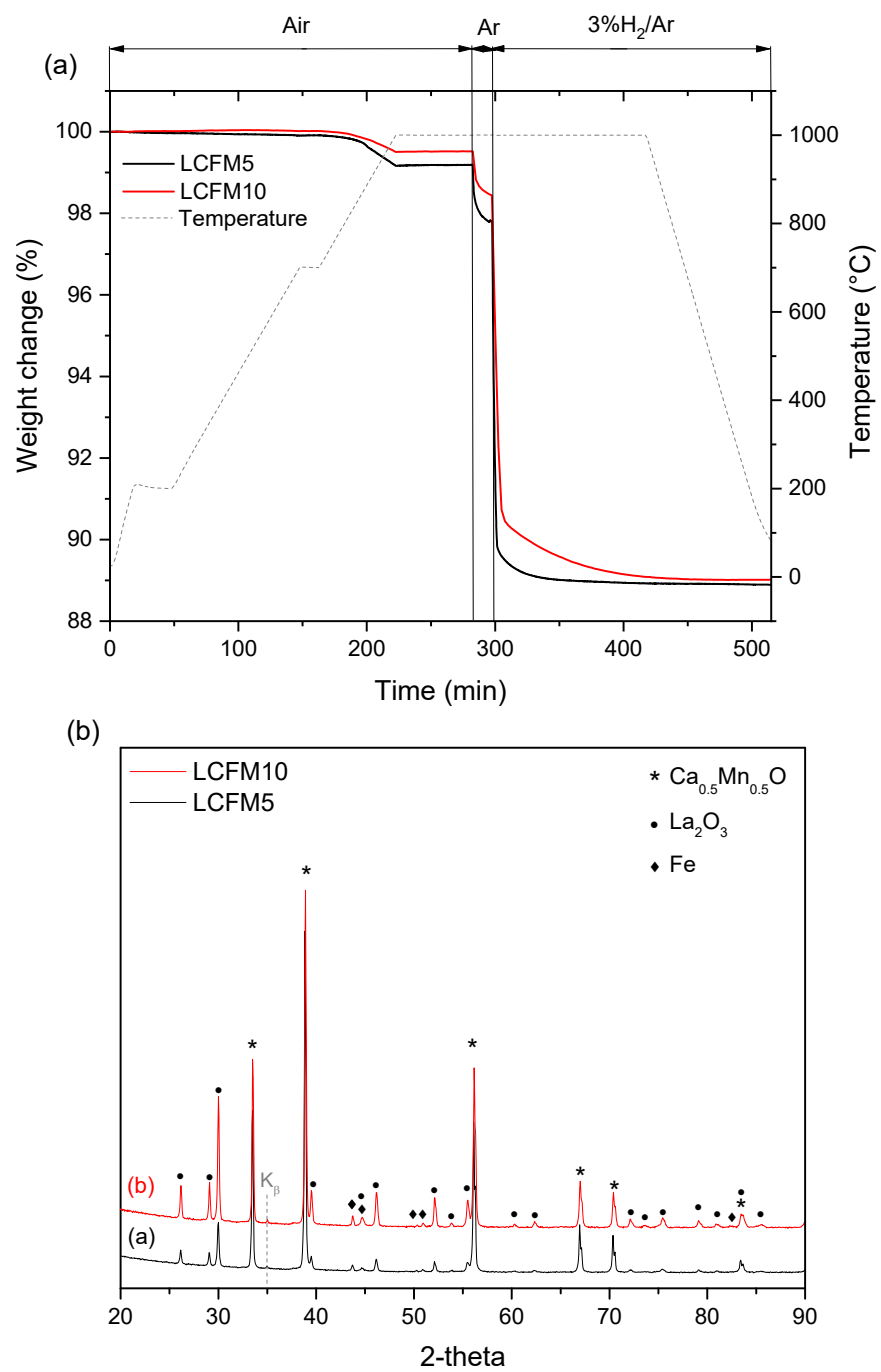
Figure S 6. (a) TGA analysis under 3% H_2/Ar. (b) XRD patterns after TGA analysis.

Table S 3. Mn, Fe, La oxidation states (z^+_M) of the as-prepared materials. z^+_{Mn} oxidation state by TG analysis was calculated considering Fe and La in 3+ oxidation state. z^+_M for M=Mn, La, Fe by XANES analysis was evaluated by edge energy shift with respect to reference materials.

	TGA	XANES					
Material	z^+_{Mn}	**Mn K-edge (eV)**	z^+_{Mn}	**Fe K-edge (eV)**	z^+_{Fe}	**La K-edge (eV)**	z^+_{La}
$CaMnO_3$	3.997	6555.56	3.997	-	-	-	-
LCFM5	3.999	6555.66	4.000	7126.61	3.116	5482.82	3
LCFM10	4.000	6555.68	4.005	7126.52	3.103	5482.81	3
$LaFeO_3$	-	-	-	7126.57	3.109	5483.04	3

5. EXAFS data analysis

As is standard, the following equation was used to model the EXAFS:

$$\chi = \sum_i \chi_i(k)$$
(1Sa)

$$\chi_i(k) = \frac{(N_i S_0^2) f(k) e^{-2k^2\sigma^2}}{2kR_i^2} \sin[2kR_i + \delta_i(k)]$$
(1Sb)

where $f_i(k)$, the scattering amplitude, and $\delta_i(k)$, the phase-shift, are photo-electron scattering properties of the neighboring atom and depend on atomic number Z. Using these known, the following parameters can be determined from the EXAFS data:

- S_0^2, amplitude reduction factor,

- R_i, distance to neighboring atom,

- N, coordination number,

- σ^2, mean-square disorder of neighbor distance.

In the Demeter software is included a FEFF program, which enables the calculation of multiple scattering from CIF files in order to simulate XAFS spectra. However, the program is not capable of writing an appropriate FEFF file for a doped material. For taking into account the dopants in the model for the oxides in this study, a $CaMnO_3$ CIF file was modified according to the guide lines provided by the Demeter software developer[4]. Specifically, the lattice parameters obtained from the Rietveld refinement were used, and the Ca and Mn atoms were partially substituted with La and Fe in accord with the material compositions. The first four obtained FEFF paths are plotted in **Figure S 7**a and **Figure S 7**b. Both first-shell and three-shell fitting models were examined. For the three-shell model fitting, S_0^2 and E_0 were constrained to reduce the number of variables to 11 with 13.17 independent points. The first-shell models captured the B-O behavior, **Figure S 7**c-f, but not the longer range features. All features were satisfactorily well captured using the three-shell fitting models. The crystallographic quantities obtained from the fitting (three-shell fitting models) are summarized in **Tables S4 – S7**. Comparison of the k^3-weighted $\chi(k)$ functions for LCFM5 and LCFM10 are presented in **Figure S 7**.

Table S 4. Mn-local structure on LCFM5 oxide as derived from EXAFS analysis.

SS	R-factor	N	S_0^2	σ^2 (Å^2)	E_0 (eV)	R (Å)
Mn-O$_1$	0.0078	6	0.911	0.0017	0.664	1.92
Mn-Ca	0.0185	2	0.911	0.0161	0.664	3.25
Mn-La	0.0185	1	0.911	0.0073	0.664	2.81
Mn-Mn	0.0185	4	0.911	0.0101	0.664	3.96

Table S 5. Mn-local structure on LCFM10 oxide as derived from EXAFS analysis.

SS	R-factor	N	S_0^2	σ^2 (Å^2)	E_0 (eV)	R (Å)
Mn-O$_1$	0.0151	6	0.992	0.0022	-4.048	1.90
Mn-Ca	0.0107	2	0.992	0.0043	-4.048	3.22
Mn-La	0.0107	1	0.992	0.0170	-4.048	3.39
Mn-Mn	0.0107	4	0.992	0.0099	-4.048	4.03

Table S 6. Fe-local structure on LCFM5 oxide as derived from EXAFS analysis.

SS	R-factor	N	S_0^2	σ^2 (Å^2)	E_0 (eV)	R (Å)
Fe-O$_1$	0.0189	6	0.973	0.0005	-5.981	1.94
Fe-Ca	0.0214	2	0.973	0.0004	-5.981	3.18
Mn-La	0.0214	1	0.973	0.0035	-5.981	2.73
Fe-Mn	0.0214	4	0.973	0.0023	-5.981	3.90

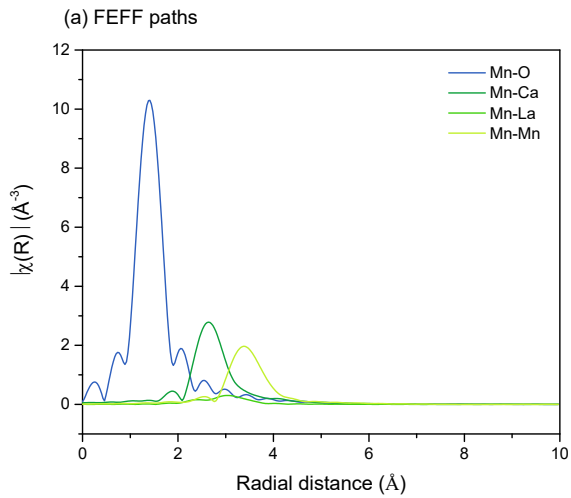**Table S 7.** Fe-local structure on LCFM10 oxide as derived from EXAFS analysis.

SS	R-factor	N	S_0^2	σ^2 (Å^2)	E_0 (eV)	R (Å)
Fe-O$_1$	0.0192	6	0.981	0.0007	-4.781	1.94
Fe-Ca	0.0166	2	0.981	0.0003	-4.781	3.20
Fe-La	0.0166	1	0.981	0.0054	-4.781	2.75
Fe-Mn	0.0166	4	0.981	0.0060	-4.781	3.91

(a) FEFF paths

(b) FEFF paths
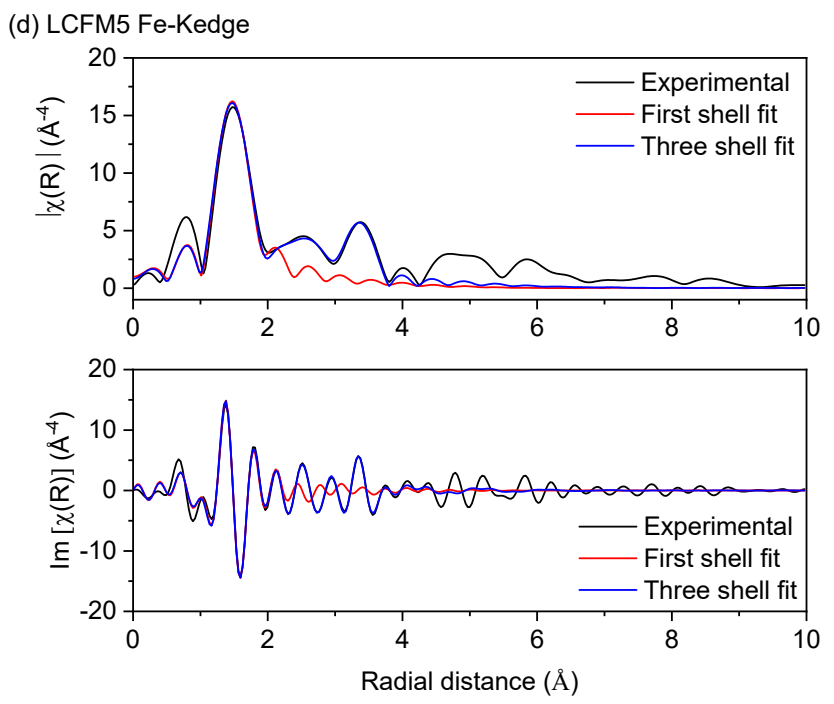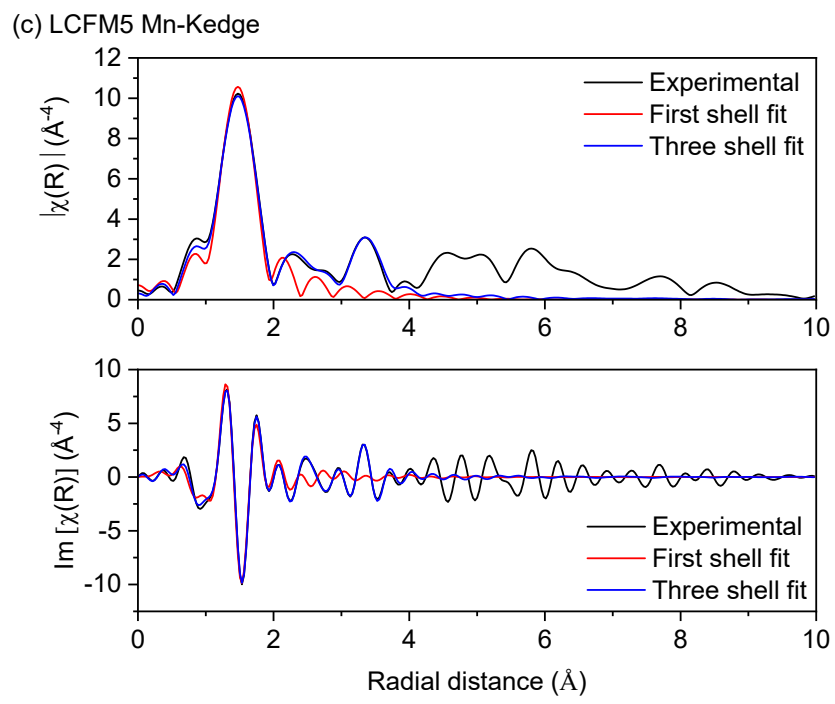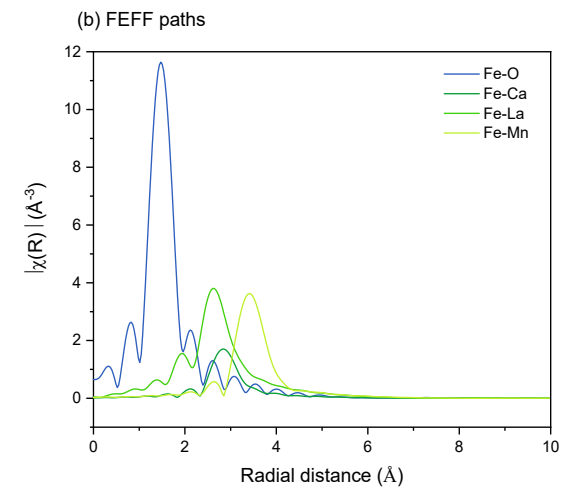
(c) LCFM5 Mn-Kedge
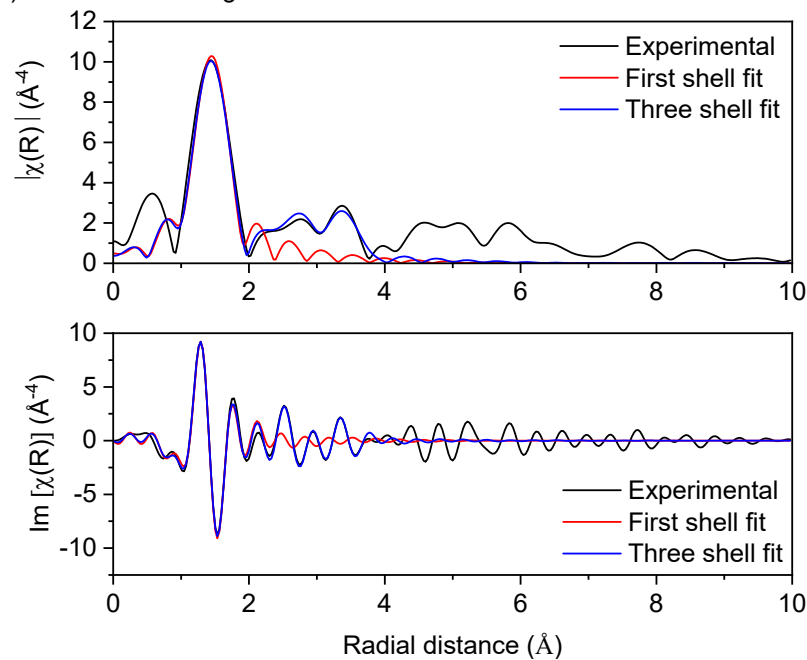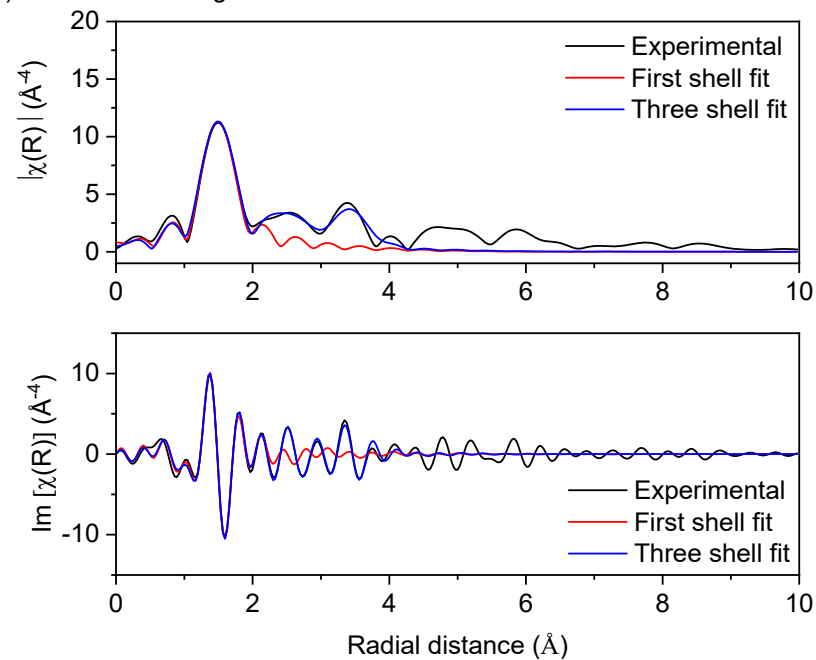
(d) LCFM5 Fe-Kedge

Figure S 7. Local structure: (a,b) paths included in the fitting model calculated by FEFF; (c-f) Fourier transforms (FT), with module ($|\chi(R)|$) and imaginary part ($Im[\chi(R)]$) of Mn and Fe EXAFS spectra of LCFM5 and LCFM10, as indicated.
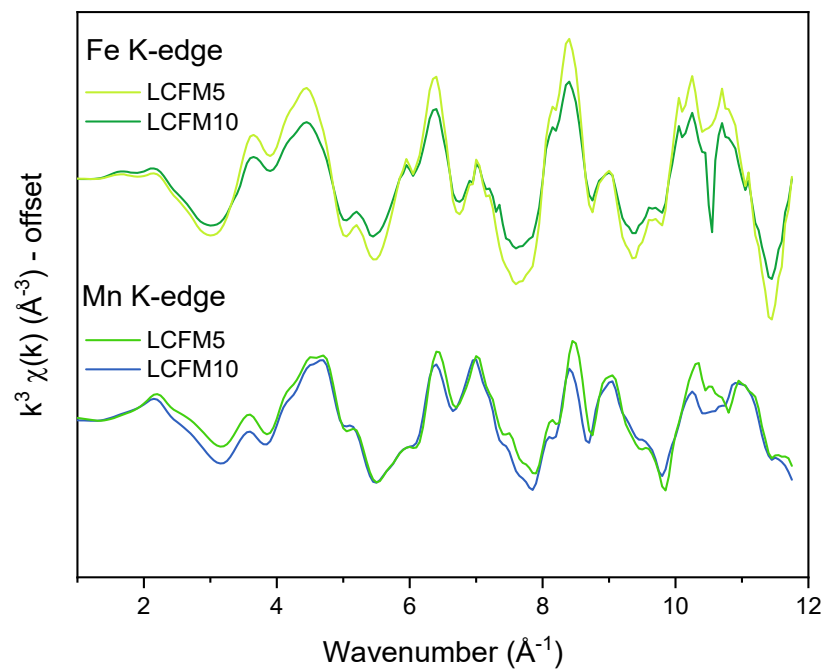
Figure S 8. Comparison of experimental EXAFS functions χ(k) for LCFM5 and LCFM10 materials weighted by k^3.

6. Phase transition

The comparison between $d\delta/dT$ and DSC profiles under a pO_2 of 0.18 atm for LCFM5 and LCFM10 shows that the thermal events detected by DSC clearly correspond to sudden mass changes, *i.e.* peaks in $d\delta/dT$ profiles. Moreover, the introduction of La and Fe into CM causes the two transitions to merge into a single step for dopants amount equal to 10 at.%. For a given material, the $d\delta/dT$ profile collected under $pO_2 = 0.18$ atm (5 °C/min) coincides rather closely with the DSC profile collected under the same pO_2 (10 °C/min), indicating the validity of the method for evaluating the phase boundaries.
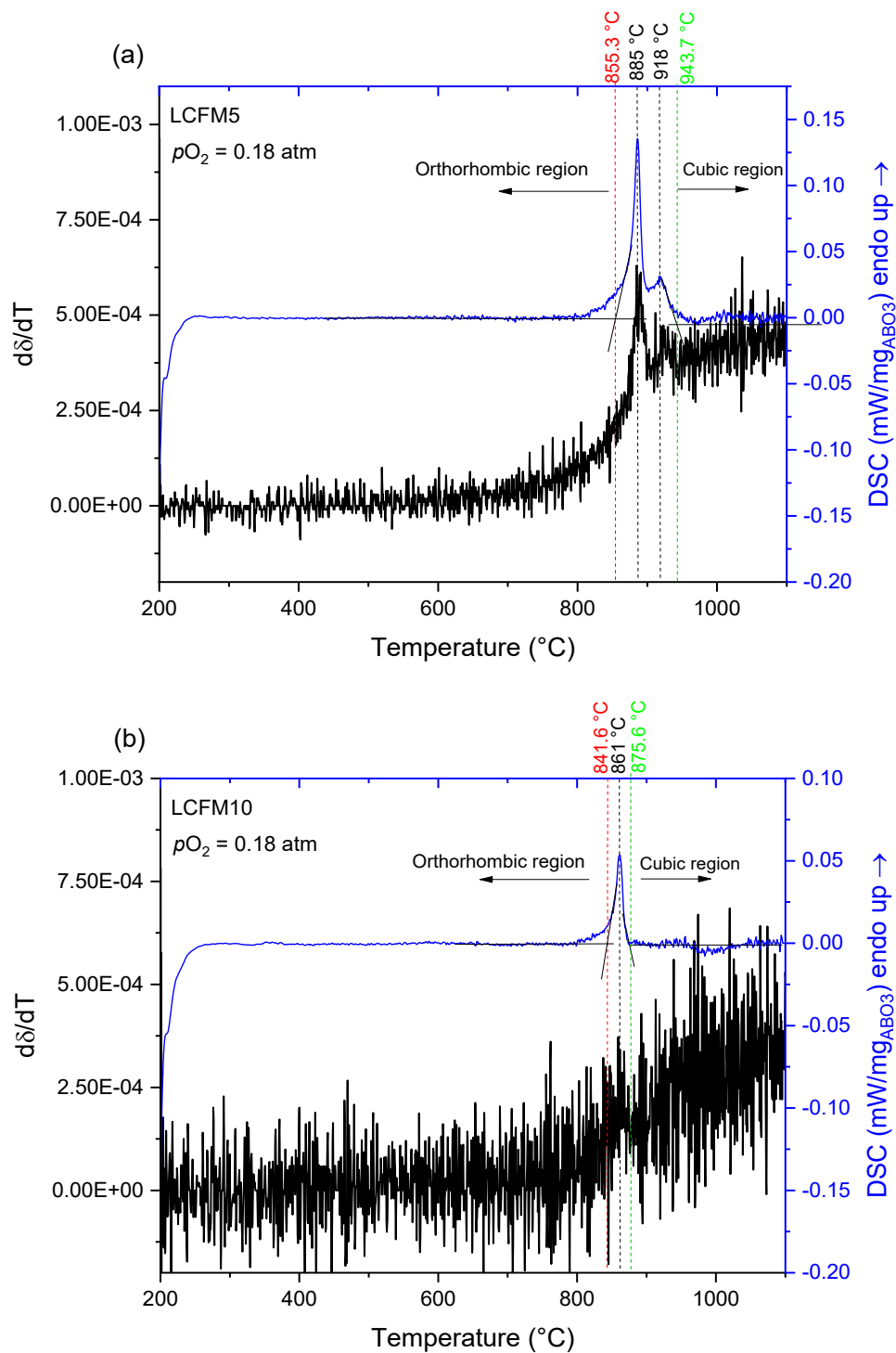
Figure S 9. dδ/dT and DSC profiles under a pO_2 of 0.18 atm for (a) LCFM5 and (b) LCFM10.

The enthalpy values relative to the phase change from the orthorhombic to cubic structure are reported in the following Table:

Table S 8. Phase change enthalpy values measured from DSC signals.

| Code | pO₂=0.18atm | | | | | | pO₂ 5·10⁻⁴ atm | | | |
| | 1st peak T_{peak} (°C) | 2nd peak T_{peak} (°C) | 1st peak ΔH (kJ/kg$_{ABO3}$) | 2nd peak ΔH (kJ/kg$_{ABO3}$) | Δδ* | ΔH (kJ/mol$_O$) | 1st peak | | | |
							T_{peak} (°C)	ΔH (kJ/kg$_{ABO3}$)	Δδ*	ΔH (kJ/mol$_O$)
LCFM5	885.3	918.2	13.8	3.5	0.049	51.6	827	14.2	0.094	22.2
LCFM10	861.1	-		4.0	0.009	67.9	814	4.2	0.047	13.4

*Δδ = δ$_{cubic}$ - δ$_{orthorhombic}$ at the transition

7. Evolution of lattice parameters with temperature

The refined lattice parameters of LCFM5 and LCFM10 for each temperature scan are listed in the following Tables:

Table S 9. Refined lattice parameters of LCFM5 for each temperature scan.

Temperature (°C)	Phase Identified	Stucture	Space Group	Lattice parameters		
				a (Å)	b (Å)	c (Å)
r.t.	$CaMnO_3$	orthorhombic	Pnma	5.2977 (8)	7.4843 (11)	5.2887 (7)
300	$CaMnO_3$	orthorhombic	Pnma	5.3103 (2)	7.5154 (7)	5.3027 (3)
350	$CaMnO_3$	orthorhombic	Pnma	5.3139 (3)	7.5194 (3)	5.3055 (4)
400	$CaMnO_3$	orthorhombic	Pnma	5.3156 (6)	7.5256 (5)	5.3105 (5)
450	$CaMnO_3$	orthorhombic	Pnma	5.3203 (6)	7.5283 (5)	5.3111 (5)
500	$CaMnO_3$	orthorhombic	Pnma	5.3234 (8)	7.5338 (6)	5.3155 (7)
600	$CaMnO_3$	orthorhombic	Pnma	5.3308 (5)	7.5431 (5)	5.3214 (5)
700	$CaMnO_3$	orthorhombic	Pnma	5.3375 (11)	7.5544 (8)	5.3294 (9)
800	$CaMnO_3$	**orthorhombic**; cubic	**Pnma**; Pm-3m	**5.3436 (8)**; 3.7795 (4)	**7.5666 (6)**; 3.7795 (4)	**5.3366 (7)**; 3.7795 (4)
850	$CaMnO_3$	**orthorhombic**; cubic	**Pnma**; Pm-3m	**5.3490 (9)**; 3.7889 (2)	**7.5775 (7)**; 3.7889 (2)	**5.3397 (8)**; 3.7889 (2)
900	$CaMnO_3$	**orthorhombic**; cubic	**Pnma**; Pm-3m	**5.3518 (9)**; 3.7941 (3)	**7.5856 (6)**; 3.7941 (3)	**5.3418 (8)**; 3.79415 (3)
1000	$CaMnO_3$	cubic	Pm-3m	3.8037 (3)	3.8037 (3)	3.8037 (3)
1100	$CaMnO_3$	cubic	Pm-3m	3.8157 (5)	3.8157 (5)	3.8157 (5)
1200	$CaMnO_3$	cubic	Pm-3m	3.8270 (3)	3.8270 (3)	3.8270 (3)

Table S 10. Refined lattice parameters of LCFM10 for each temperature scan.

Temperature (°C)	Phase Identified	Stucture	Space Group	Lattice parameters		
				a (Å)	b (Å)	c (Å)
r.t.	CaMnO$_3$	orthorhombic	Pnma	5.3269 (6)	7.5197 (14)	5.3173 (9)
300	CaMnO$_3$	orthorhombic	Pnma	5.3386 (8)	7.5420 (10)	5.3323 (12)
350	CaMnO$_3$	orthorhombic	Pnma	5.3419 (1)	7.5463 (4)	5.3357 (8)
400	CaMnO$_3$	orthorhombic	Pnma	5.3456 (5)	7.5507 (5)	5.3381 (2)
450	CaMnO$_3$	orthorhombic	Pnma	5.3488 (11)	7.5551 (8)	5.3415 (3)
500	CaMnO$_3$	orthorhombic	Pnma	5.3526 (6)	7.5597 (5)	5.3447 (4)
600	CaMnO$_3$	orthorhombic	Pnma	5.3602 (2)	7.5698 (5)	5.3509 (3)
700	CaMnO$_3$	orthorhombic	Pnma	5.3678 (9)	7.5813 (10)	5.3587 (3)
800	CaMnO$_3$	**orthorhombic**; cubic	**Pnma**; Pm-3m	**5.3735 (5)**; 3.79943 (4)	**7.5914 (7)**; 3.79943 (4)	**5.3646 (3)**; 3.79943 (4)
850	CaMnO$_3$	cubic	Pm-3m	3.80594 (2)	3.80594 (2)	3.80594 (2)
900	CaMnO$_3$	cubic	Pm-3m	3.81207 (2)	3.81207 (2)	3.81207 (2)
1000	CaMnO$_3$	cubic	Pm-3m	3.82342 (3)	3.82342 (3)	3.82342 (3)

| 1100 | CaMnO$_3$ | cubic | Pm-3m | 3.83634 (5) | 3.83634 (5) | 3.83634 (5) |
| 1200 | CaMnO$_3$ | cubic | Pm-3m | 3.84956 (3) | 3.84956 (3) | 3.84956 (3) |

8. pO_2 sensor data

The oxygen sensor recorded for both materials small variations of pO_2 value over the course of the experiment with the exception of phase change events.
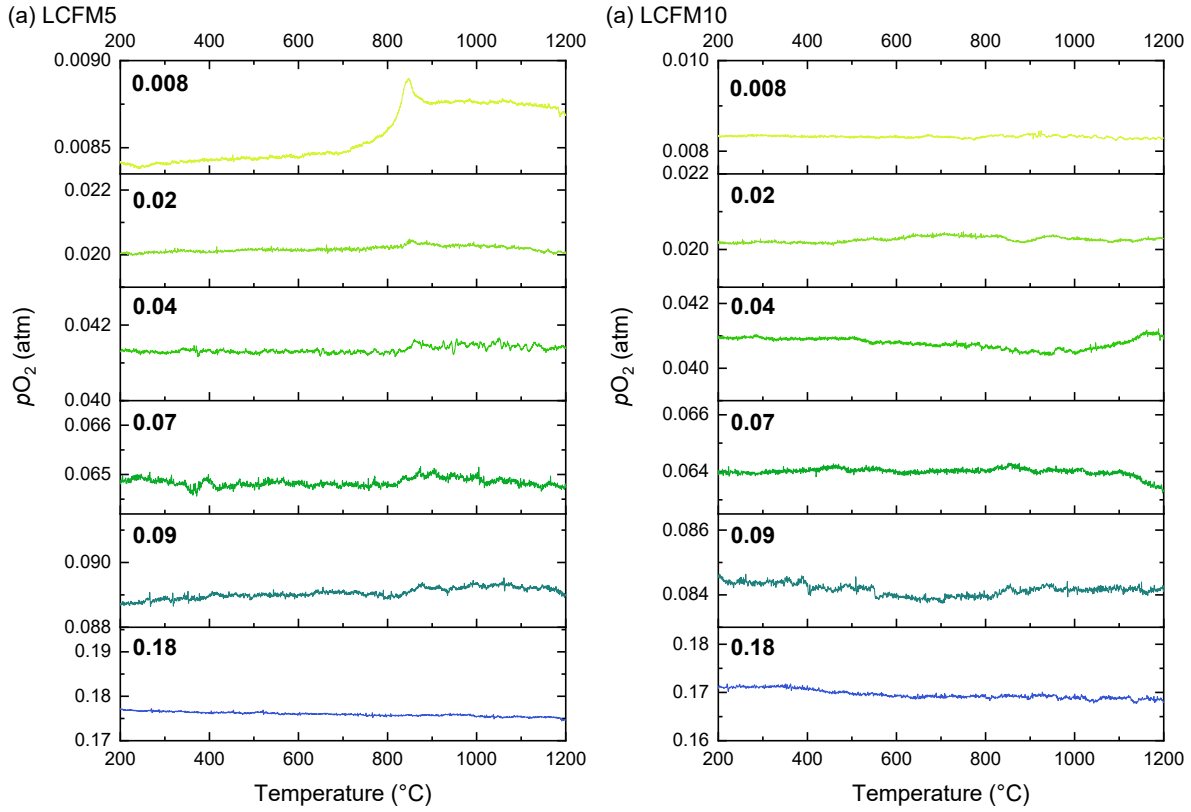

Figure S 10. $pO_2(T)$ profiles of (a) LCFM5 and (b) LCFM10. Boldtype number indicates nominal inlet oxygen partial pressure supplied during the measurement.

9. δ(T) profiles under 0.004 atm

The δ(T) profiles of LCFM5 and LCFM10 measured under continuous heating and a pO_2 of 0.004 atm (methods identical to those reported in the main text for higher pO_2 conditions) are reported here (**Figure S 11**). It can be seen that for both materials, the heating (solid red line) and the cooling (blue dashed line) curves differ slightly, indicating that the measurements deviated slightly from equilibrium conditions. Accordingly, these data were not used for the determination of the thermodynamic functions, $\Delta \bar{H}_O^0(d)$ and $\Delta \bar{S}_O^0(d)$; instead (as noted in the main text), only the δ(T) data sets in the pO_2 range 0.18-0.008 atm were used. To assess the behavior at 0004 atm, the expected equilibrium δ(T) profile under this pO_2 was calculated using the thermodynamic functions (assuming a fixed $\Delta \bar{H}_O^0(d)$ and a linear $\Delta \bar{S}_O^0(d)$ at high δ). For both materials, the calculated δ(T) profiles at 0.004 atm almost perfectly overlap with the experimental heating curve. This suggests that the materials were in equilibrium conditions while heating but not during the cooling measurement. This can be explained considering that thermokinetic limits are more severe during oxidation in an O_2 poor gas due to the low driving force than they are during reduction when the driving force is high.
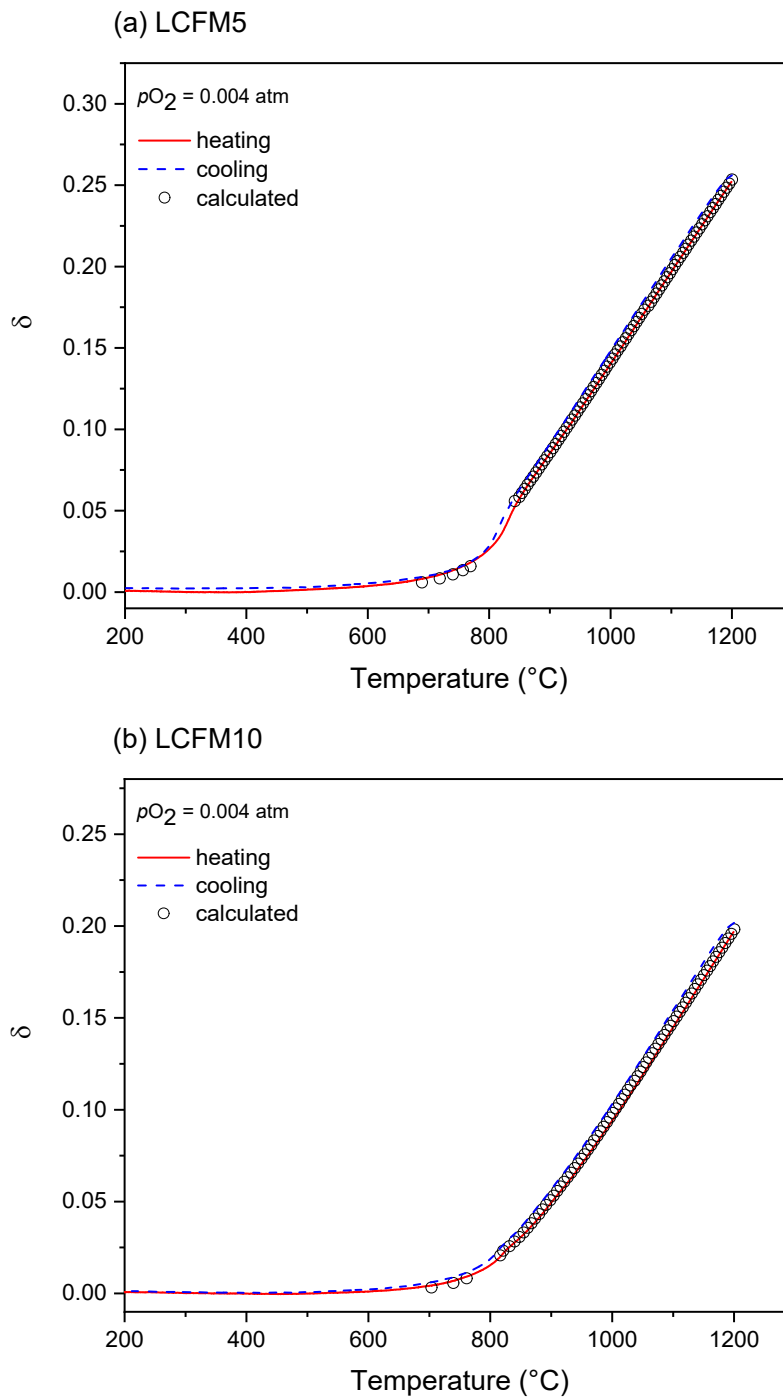
(a) LCFM5

(b) LCFM10

Figure S 11. Heating (red solid line) and cooling (blue dashed line) $\delta(T)$ profiles measured under pO_2 = 0.004 atm for (a) LCFM5 and (b) LCFM10. The symbols correspond to the calculated δ from the thermodynamic data reported in Figure 11.

10. dδ/dT profiles

A significant feature of all of the mass loss (and hence non-stoichiometry) profiles is the evidence of a discontinuity at the crystallographic phase transition(s). This effect, which is particularly pronounced in undoped $CaMnO_3$,[5] reflects the difference between the maximum δ in the orthorhombic phase and the minimum δ in the higher temperature phase (either tetragonal or cubic) at the pO_2 of the measurement. The position of the anomaly in the dδ/dT profiles thus reflects the phase transition temperature. Good agreement is observed between this method of phase transformation detection and traditional DSC methods (Figure S 8), with the mass analysis providing the benefit of greater sensitivity.
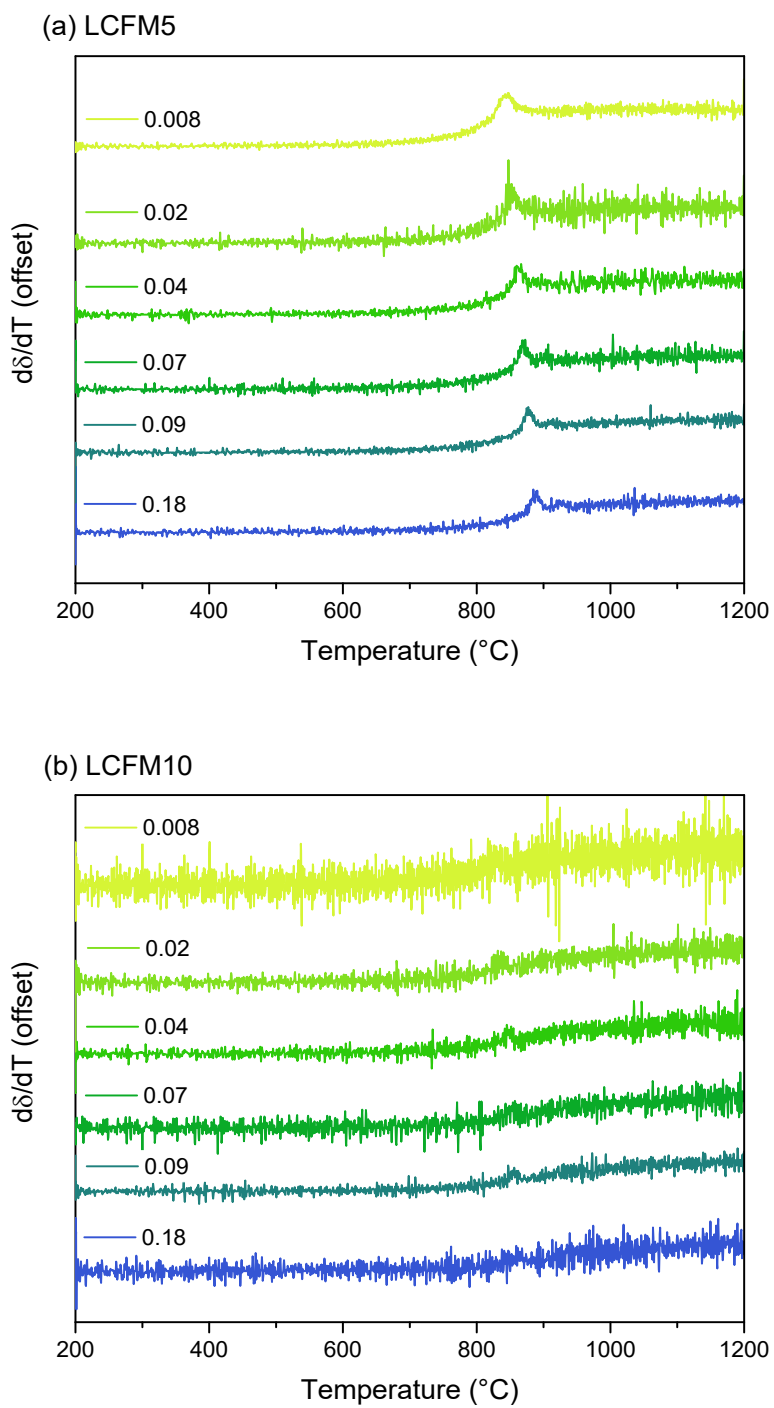
(a) LCFM5

0.008
0.02
0.04
0.07
0.09
0.18

(b) LCFM10

0.008
0.02
0.04
0.07
0.09
0.18

Figure S 12. dδ/dT profiles of (a) LCFM5 and (b) LCFM10.

11. Phase behavior of LCFM compositions

The phase boundary information across all measurement conditions were combined and used to construct pO_2-T phase stability diagrams for the $(La_xCa_{1-x})(Fe_xMn_{1-x})O_3$ materials.
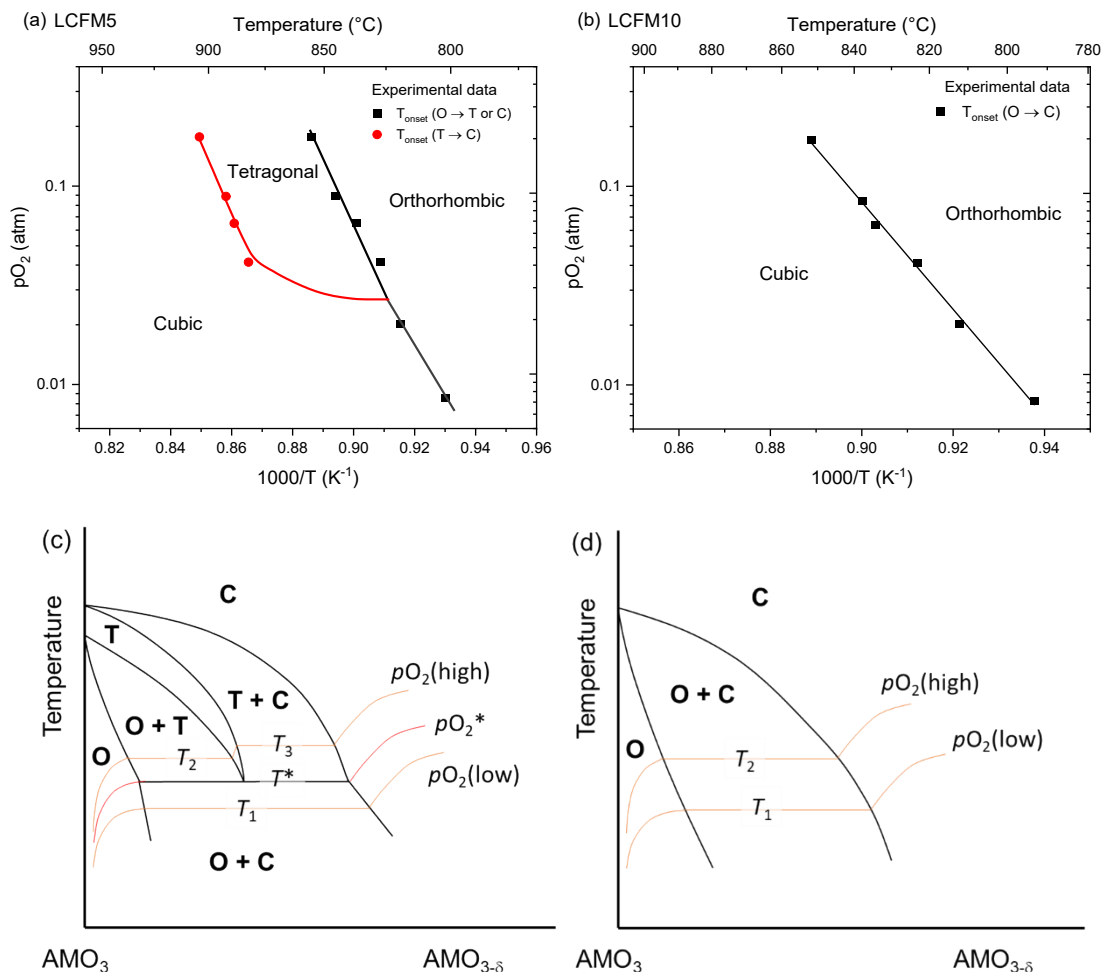

Figure S 13. Phase behavior of (a,c) LCFM5 and (b,d) LCFM10 in the form of (a,b) stability diagrams and (c,d) phase diagrams, showing the pO$_2$-T regions over which the orthorhombic, tetragonal, and cubic phases, occur. Lines in (a) are guides to the eye, indicating plausible boundaries, whereas datapoints are measured; the line in (b) is a linear fit to the measured datapoints. Figures in (c,d) are schematic, and iso-baric curves indicate the phase(s) present at the given pO$_2$. In (c) pO$_2$* and T* indicates the triple point oxygen partial pressure and temperature at which cubic, tetragonal, and orthorhombic phases coexist at equilibrium.

The stability diagrams reflect the observation that high temperature and low oxygen partial pressure conditions favor the cubic phase, whereas the orthorhombic phase is favored at low temperatures and high oxygen partial pressures. In agreement with DSC (Figure 7 and Figure 8) and *in situ* XRD analysis (Figure 5), the widths of the two-phase regions decreases as the dopant content increases from 5 to 10% at. The disappearance of the tetragonal phase at low pO_2 from the stability diagram of LCFM5 and at all measured pO_2 from the stability diagram of LCFM10 is captured in the schematic phase diagrams.
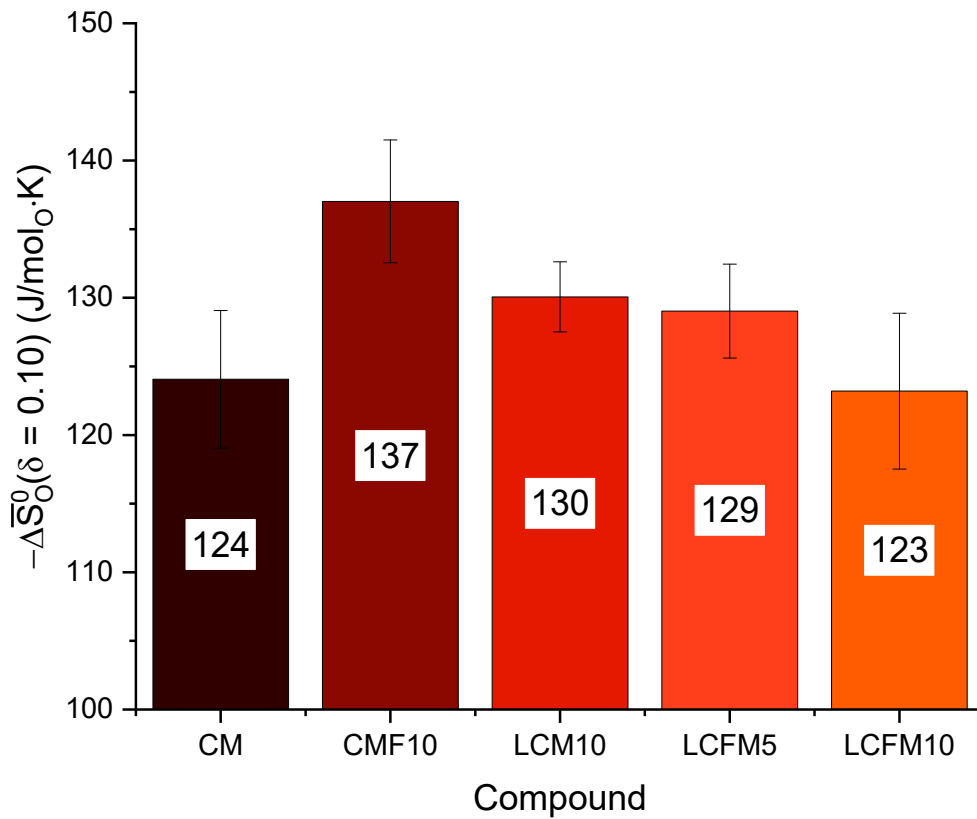

Figure S 14. Comparison of partial molar entropy of oxygen in $CaMnO_3$-based materials at $\delta = 0.10$.

12. Heat storage capacity comparison

Table S 11. Comparison of LCFM5 and LCFM10 with previously investigated compositions CM, CMF10 and LCM10 under similar operating conditions (pO_2=0.008 atm, T_{dis}=700°C, T_{ch}=1200 °C)

	$pO_2 = 0.008$ atm					
Code	Selected Operating T range (°C)	ΔT (°C)	Dd	Q_M (kJ/kg)	Q_v (kWh/m³)	Accessible Operating T range (°C)
CM	700-1100*	400	0.23	273	366	700-1100
LCM10	800-1200	400	0.20	265	354	800-1200
CMF10	700-1200	500	0.24	303	405	400-1200
LCFM5	700-1200	500	0.23	291	398	700-1200
LCFM10	700-1200	500	0.18	231	303	700-1200

*CM above 1100 °C decomposes into the spinel ($CaMn_2O_4$) and Ruddlesden – Popper (Ca_2MnO_4) phases.

Bibliography

1   Z. You, M. K. Paek and I. H. Jung, *J Phase Equilibria Diffus*, 2018, **39**, 650–677.

2   B. Fubini and F. S. Stone, *Journal of the Chemical Society, Faraday Transactions 1: Physical Chemistry in Condensed Phases*, 1983, **79**, 1215–1227.

3   S. Sasaki, K. Fujino and Y. Takeuchi, *Ser. B*, 1979, **55**, 43–48.

4   B. Ravel and M. Newville, *J Synchrotron Radiat*, 2005, **12**, 537–541.

5   E. Mastronardo, X. Qian, J. M. Coronado and S. M. Haile, *J Mater Chem A Mater*, 2020, **8**, 8503–8517.